Numerical and experimental investigations into protection net icing at the helicopter engine inlet

Abstract

Purpose – The main purpose of this paper is to numerically and experimentally evaluate the effect of the protection net icing on the inlet performance of helicopter engines.

Design/methodology/approach – The ice shapes of the protection net at different times are firstly simulated by a 2D icing calculation, then the porous media parameters are calculated based on the 2D ice shapes. Afterwards, a three-dimensional (3D) flow fields of the engine inlet with the iced net are simulated using the porous media model instead of the real protection net. The transient pressure losses of the iced protection net are calculated and tested through an icing wind tunnel test rig under different icing conditions.

Finding – Overall the numerical results and experimental data shows a good agreement. The effects of several control parameters such as liquid water contents (LWC), water droplet diameters, and airflow velocities on the pressure loss of the protection net during the icing process are analyzed in a systematic manner. The results indicate that the pressure loss increases with the increase of the LWC at the same icing time. The same trend occurs when the water droplet diameter and the airflow velocity increase.

Originality/value – A new method to predict the pressure loss of the iced protection net is proposed. A series of tests in an icing wind tunnel are performed to obtain the ice shapes and pressure loss of protection net during icing process.

Keywords Icing simulation, Porous medium model, Pressure loss, Icing wind tunnel

Paper type Research paper

1. Introduction

It is recognized that the air intake protection net can prevent turbine engine intakes from ingesting foreign objects such as leaves, bird, etc, which might have a catastrophic impact on engine (Wilcox et al. 2012). However, the protection net icing at engine inlet will lead to pressure loss of air flow that will significantly affect the performance of the engine. Therefore, it is imperative to study the icing of protection net.

Over the past several decades, many efforts were devoted to research on icing using different methodologies such as icing wind tunnel experiments, flight experiments, and numerical simulation. In the aspect of icing experiments, Ikiades et al (2013) proposed a new approach to ice detection based on developments of Mie scattered and reflected light technology. Their research can provide the thickness and type information of ice accretion on aerodynamic surfaces, and it would be valuable for the design and development of optical direct ice detection sensor for aerospace application. Gao et al. (2019) carried out an experimental study of the icing process on a typical wind turbine airfoil model in an icing tunnel. The high-resolution image results indicated that, due to the backflow of impinging water on the surface, the growth rate of ice accretion along the leading edge of airfoil under glaze icing condition was much slower than that under the mixed and rime icing conditions. Li et al. (2019) investigated the dynamic icing and non-steady heat transfer process on the icing composite fuselage surface. They found that the thermal conductivity of airframe substrate had a significant effect on the unsteady heat transfer processes and dynamic ice accretion over the ice accretion surfaces. Besides, the icing process of a planar stainless steel protection grids in use on rotorcraft and turboprop engines were experimental studied by Vercillo et al (2019). A general physical model for that was proposed, which can be used to calculate the variation of grid blockage and pressure loss with time. Jin et al. (2020) experimentally analyzed the influence of icing on the aerodynamic performance of S826 and S832 airfoils for both dry and wet ice conditions. Their experimental results showed that the ice accretion was affected by the geometric characteristics of the airfoil. Compared with the S826 airfoil, the ice shape of the S832 airfoil was more complex and its aerodynamic performance had a higher change. The above icing experimental researches provided an efficient support for the theoretical development and numerical simulation of icing.

Compared with the icing wind tunnel experiment, icing simulation has the advantages of lower cost and faster speed. Numerical simulation on icing have been widely studied for many years (Du et.al., 2010; Verdin et al., 2013; Pouryoussefi et al.,2016; Raj et al., 2019). With the machine learning theory, the icing on the NACA0012 two-dimensional wing surface with the combination method of WPT and ANN was calculated by using neural network and wavelet transfer (Chang et al. 2016). Based on the fundamental theory of solid-liquid phase change, a new one-dimensional aircraft icing model was proposed regarding rime ice as porous media, which provided an alternative approach for icing simulation (Zhang et al, 2017). In addition, Groth et al. (2019) proposed a new method to update the numerical grid of icing shape, which can be combined with CFD analysis to achieve the dynamic growth of icing. Their results showed that the method was quite universal and it can be used in all CFD solver and optimization

programs when the position of mesh nodes was modifiable. Son et al. (2020) developed a wind turbine icing simulation code with performance evaluation (WISE) to calculate the icing on rotating wind turbines. However, their code cannot predict the flow transition on the lower Reynolds region. Based on machine learning method, the maximum thickness, icing area and icing severity level of aircraft icing were predicted (Li et al, 2020). The results showed the method had a reasonable capability to evaluate the icing severity.

During the flight, the protection net at the helicopter engine inlet may freeze. In the previous studies, porous media model was usually used to simplify the net-like structures as the iced protection net. Castellano et al. (2016) tested the flow parameters of airflow through fifteen agricultural nets and obtained empirical equations related to porosity. The computational results were in good agreement with the experimental data except for higher porosity nets. Cheung et al. (2019) simulated the natural convection in porous media combining proper orthogonal decomposition model and deep learning concept. Their results showed the flow rate in heterogeneous porous media can be well approximated with the numerical method. Pashchenko et al. (2019) studied the pressure drop and loss factor of porous packed bed by using ANSYS Fluent. The error of pressure loss between their numerical and the experimental results was less than 8% and that showed a good correlation. Besides, a CFD model for perforated porous media was proposed by Movahedi et al (2020). Under steady-state conditions, the pressure drop changes of an air–water along clean and gravel-filled perforations system were successfully predicted by the model. Using porous media model, Montoya et al. (2020) simulated the pressure drop of air flowing through the fog water collector. The porous media model was proved to be an effective model by comparing with the results of direct simulation.

It is aforementioned from previous studies that there is still a lack of in-depth study on the icing simulation of net-like structures, especially for convex net-like structures. Thus, the current work aims to develop a new numerical method to simulate the icing shapes of 2D protection net structures with the multi-step method and predict the pressure loss caused by the 3D protection convex net icing according to a porous media model. In the present work, icing wind tunnel experiments are carried out to observe the ice shape and to obtain the pressure loss. Correspondingly, the 2D simplification and 3D flow field simulation of the protection net icing with the same icing conditions are addressed. The ice shapes and the pressure losses resulted from the icing wind tunnel experiments are presented and compared with the simulated data. Moreover, another major contribution of the current work is to investigate the effects of several different icing parameters such as liquid water contents (LWCs), diameters of water droplets, and airflow

velocities on the pressure loss. This study will be very helpful in providing guidance on the effect of icing on the airflow of net-like structures.

2. Icing wind tunnel experiments

Icing wind tunnel experiments on the protection net icing were carried out at China Aerodynamics Research and Development Center, China. The icing wind tunnel had a cross sectional dimension of 3 m × 2 m and it can be used for the study of cloud field parameter calibration, ice shape capture, hot gas anti-icing and electric de-icing. The calibration method and process of cloud field parameters of the icing experiments met the standard issued by American Society of Mechanical Engineers (SAE ARP5905) (2003).

2.1 Test section and pressure measuring points

Figure 1 shows the protection net in the front of the helicopter engine intake, which is made of thousands of stainless steel wires with a diameter of 0.8 mm. A rear-facing opening in the protection net is designed to allow some airflow in case of complete blockage.

Figure 1 Real model of helicopter engine inlet protection net

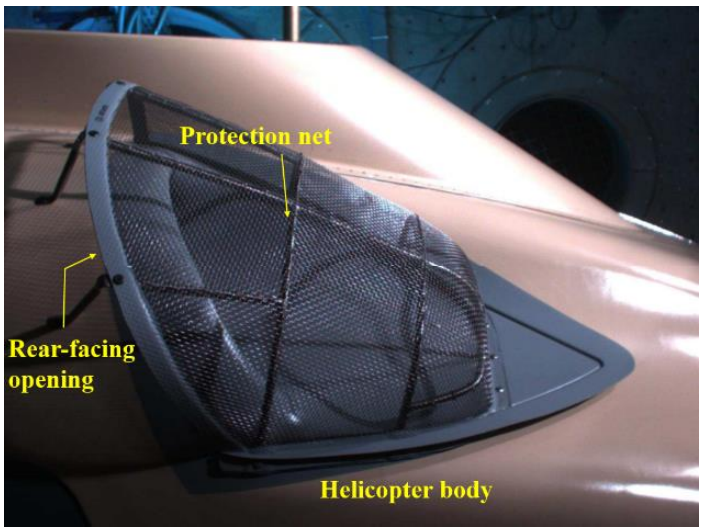

A 1:1 model of the engine inlet system including the cowling, the engine air intake, and the protection net was arranged along the center of the wind tunnel. To maintain the required mass flow rate of the engine air intake, a large-scale air extractor was used to pump the air from the wind tunnel into the engine intake. During the tests, both static and dynamic pressures at different positions inside the wind tunnel and the engine intake were measured by pressure

transducers, as shown schematically in Figure 2. The position of P1 is about 220 mm from the outlet of engine intake port and P3 is located at uniform flow field near the inlet of icing wind tunnel. There are five pressure measuring holes on P1 and P3, respectively. In this study, the total pressure loss of icing protection net is the average difference of that at the holes between P1 and P3. The air temperature was measured by thermocouple, and all the recorded test data were saved in a remote computer automatically. Unfortunately, only approximate ice shapes could be observed from the watch window on the wind tunnel during the tests due to the limitation of the conditions.

Figure 2 Position of pressure measurement in icing wind tunnel

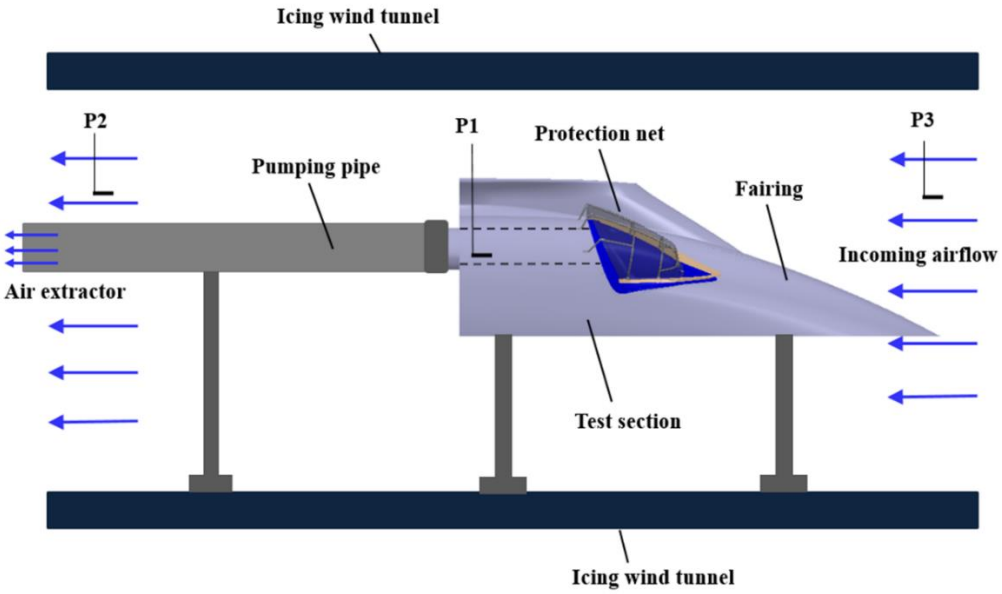

2.2 Experimental cases

Prior to the aimed tests, the required parameters such as the flight height and velocity, the ambient temperature, the LWC, the MVD, the mass flow rate of the engine, and the test time were listed for three different case studies in Table 1. During the tests, both the static and dynamic pressures at each point will be obtained in order to calculate the total pressure.

Table 1 Icing conditions of experiments and simulation

	V	*T* (℃)	LWC (g/m^3)	*H*(km)	MVD (μm)	*Q* (kg/s)	Time(s)
Case 1	11 m/s	-5	0.6	0	20	3.97	900

Case 2	280km/h	-30	0.2	6.1	20	2.15	165
Case 3	280km/h	-5	0.4	1.2	30	3.49	165

3. Numerical details

3.1 Model simplification and Method

For simulating the air flow field for the engine inlet system, it could be difficult to find an ideal simulation model for the real protection net due to the small sizes and the large quantities of the net wires. In order to obtain the pressure loss introduced by the protection net icing, the ice shapes of the protection net and the flow field of the engine intake including the protection net need to be simulated. Figure 3 illustrates the computational flow chart in predicting the pressure loss.

Figure 3 Computational flow chart in predicting the pressure loss during icing process of protection net.

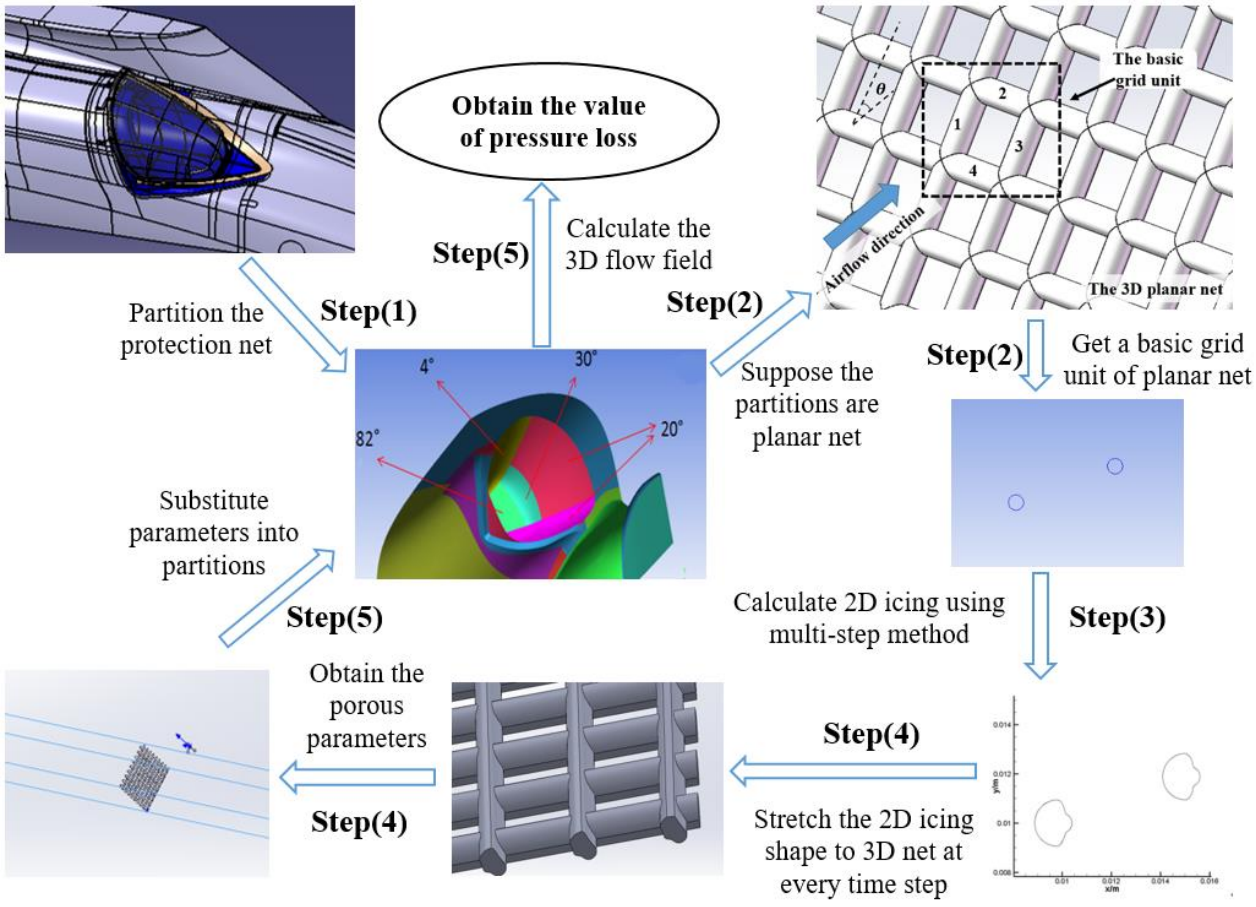

The detailed procedure in predicting the pressure loss is summarized as follows:

Step (1):

A 2D simplified model of the 3D protection net is established according to each net partition with different angles. Zones of the protection net can be treated as several approximate planes although the protection net is a spatial curved surface. Depending on the angle between approximate planes and the horizontal plane, the entire protection net can be divided into four different partitions with angles of 4°, 20°, 30° and 82°, respectively.

Step (2):

For each partition plane, the airflow through it with a certain angle can be assumed to be uniform. Consequently, as shown in Figure 3, a basic unit constituted by four mesh wires could be chosen to further simplify the icing analysis. If the direction of the airflow is perpendicular to the axial direction of wires 2 and 4, the effect of both wires on the air flow can be considered as the same. Meanwhile, the airflow direction forms a certain angle with the axial direction of wires 1 and 3, which is equal to the partition angle. Wires 1 and 3 can cause the same effect on the airflow. Therefore, 2D wire structures instead of 3D wire meshes could be assumed to calculate the ice growth. For the case of uniced protection net, wires 2 and 4 can be simplified to two circles, while wires 1 and 3 can be simplified to two ellipses. For these simplified 2D structures, icing simulation can be carried out with the multi-step method. Moreover, the simplified 2D wire structures will be different because of the difference of partitions. Figure 4 presents a 2D simplified circles and ellipses for the four different partitions. It is worth mentioning that different relative positions between both circles or both ellipses will lead to various icing shapes.

Figure 4 2D simplified circles and ellipses for different partitions

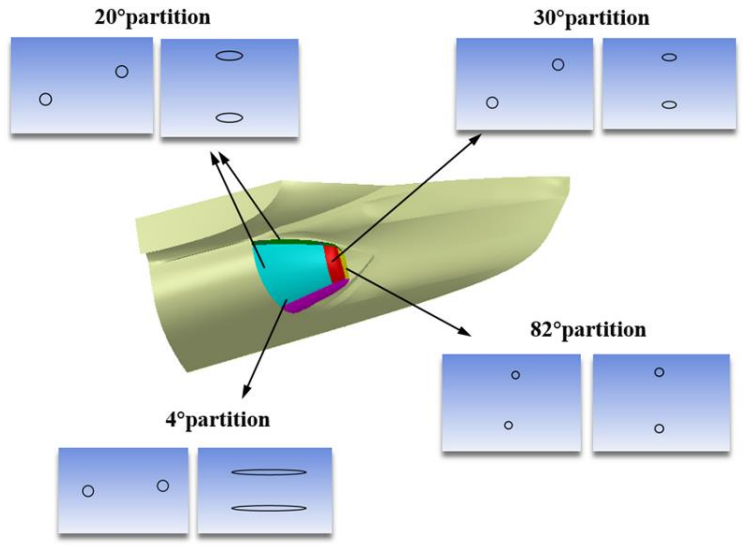

Step (3):

Based on the simplified 2D circles or ellipses, a corresponding computational domain has been built and discretized with triangular elements by ICEM CFD software. The local mesh refinement around the circles or ellipses is performed to obtain accurate results. The two-phase flow field of the air and water droplet are simulated using the method of combining Euler model with negative mass source terms in ANSYS Fluent software. Therefore, the mass of impacted water $\dot{m}_{\mathrm{im}}$ in mass conservation equation could be determined by the obtained flow field data when the Messinger model was used to simulate the icing on the circles and ellipses. During the simulations, the local collection coefficients of water droplets and the ice shapes on both circles and ellipses are calculated by the in-house program with the aid of user defined function (UDF).

Step (4):

Porous media model is used to simplify the net model. The porous media parameters such as the face permeability, the pressure-jump coefficient, and the porous media thickness can be calculated by the following method. As shown as step (4) in Figure 3, 3D planar nets can be built by directly stretching the 2D ice shapes at different time steps in SolidWorks software. It should be noted that the stretching direction of the ice shape on the circles and ellipses was crossed based on the angle of the corresponding partition. Then computational domain including 3D iced planar net was built and discretized with tetrahedral elements by ICEM CFD software. The corresponding air flow fields are simulated to calculate the pressure losses at different airflow velocities flowing through the 3D iced planar net. Furthermore, with the method introduced in help document of Fluent (2014), a fitted quadratic function of velocity can be obtained by a series of pressure losses and velocities. The porous media parameters (pressure-jump coefficient, permeability and the thickness of the medium) can be calculated by the function. These parameters need to be obtained for each partition.

Step (5):

With reasonable simplification of supporting frames and small bosses, the computational domain of 3D real protection net is built and discretized with tetrahedral elements by ICEM CFD software. As shown in Figure 5, local mesh refinement around the engine intake is carried. After independence analysis, the final economical element number is about 330,224 and the minimum orthogonal quality is 0.403. The flow field of the engine intake including the entirely iced protection net is simulated. Meanwhile, similar to the method of partitions, the 3D real protection net is considered as the combination of five porous-jump faces. The porous media parameters of each porous-jump face

are obtained from the corresponding 3D planar nets. Thus, the pressure loss caused by the protection net icing can be achieved at each icing time step. It is known that the air flow field of the engine intake can be changed by the protection net icing. Therefore, the effect of the ice shapes at different icing times on the flow field need to be taken into account. The velocity and pressure distribution in front of each partition are also obtained. They will be used as the inlet parameters to calculate the two-dimensional icing for the next time step.

Figure 5 mesh of 3D protection net

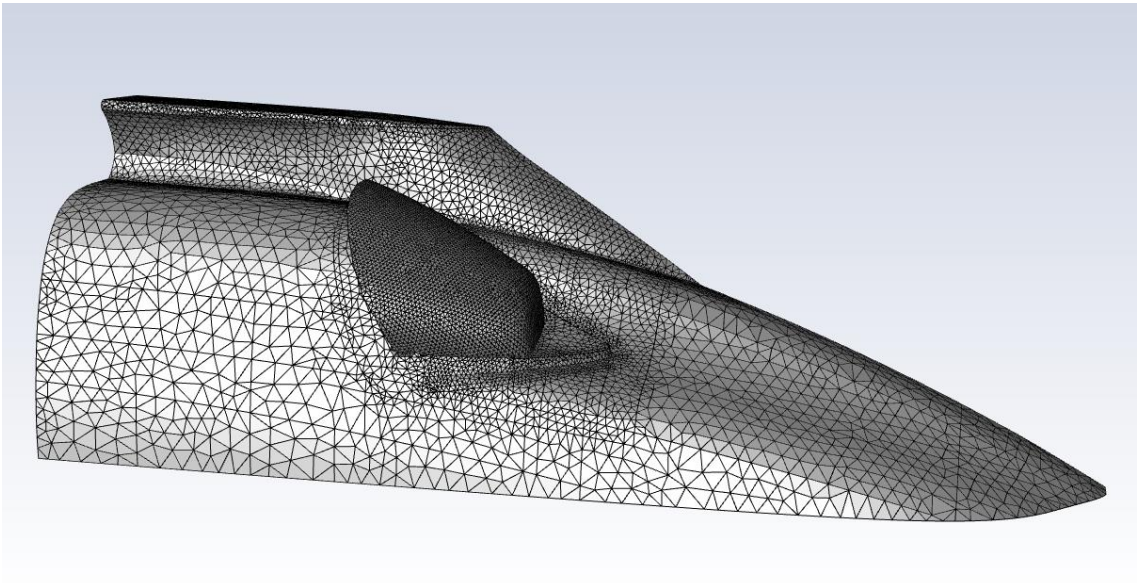

Step (6):

Above process step (1) to step (5) are only one time-step of the icing multi-step method. At the first time-step, the 2D shapes for icing simulation are original simplified circles and ellipses in corresponding partitions at step (3). And the airflow temperature and velocity at the inlet of the computational domain were approximately equal to those of the incoming airflow before the 3D protection net due to the negligible effect of the 3D net on the air flow. However, at next time-steps, the ice shape results of last time-step are used as the 2D simplified shapes to icing simulation in step (3) with the icing condition obtained at step (5). Overall, the entire icing process need to repeat steps (3), (4) and (5) to acquire the pressure loss of the iced protection net until time is over or protection net is blocking.

3.2 Governing equations

When describing the motion of water droplets in the air, they are all controlled by the basic physics conservation laws, i.e., the mass, the momentum and the energy conservation equations. They governing equations are described as

$$\frac{\partial(\rho\phi)}{\partial t} + div(\rho\vec{U}\phi) = div(\Gamma_\phi grad\phi) + S_\phi \tag{1}$$

where, ρ is represents density.$\emptyset$, $\vec{U}$, $\Gamma_\phi$and S_ϕ are generalized variable, velocity vector, diffusion coefficient and source term, respectively.

The standard k-ε model can be used to solve most turbulence problems in actual engineering, which can be described as

$$\frac{\partial}{\partial t}(\rho k)+\frac{\partial}{\partial x_i}(\rho k u_i)=\frac{\partial}{\partial x_j}[(\mu+\frac{\mu_t}{\sigma_k})\frac{\partial k}{\partial x_j}]+G_k+G_b-\rho\varepsilon-Y_M+S_k \tag{2}$$

$$\frac{\partial}{\partial t}(\rho\varepsilon)+\frac{\partial}{\partial x_i}(\rho\varepsilon u_i)=\frac{\partial}{\partial x_j}[(\mu+\frac{\mu_t}{\sigma_\varepsilon})\frac{\partial \varepsilon}{\partial x_j}]+C_{1\varepsilon}\frac{\varepsilon}{k}(G_k+C_{3\varepsilon}G_b)-C_{2\varepsilon}\rho\frac{\varepsilon^2}{k}+S_\varepsilon \tag{3}$$

where *k, ε* are the turbulent kinetic energy and turbulent energy dissipation. μ, μ_t, u_i are viscosity, turbulent viscosity and mean velocity, respectively. G_k is the generation term of *k* caused by the average velocity gradient. G_b is the additional term of *k* caused by buoyancy, and $G_\varepsilon$is the generation term of *ε* caused by the lift force. Y_M represents the contribution of pulsation expansion in compressible turbulence to the overall turbulent dissipation rate. $c_{1\varepsilon}$, $c_{2\varepsilon}$ and $c_{3\varepsilon}$ are constants, $\sigma_k$and σ_ε are the Prandtl numbers corresponding to *k* and *ε*, respectively. S_k and S_ε are the source terms defined by the user.

When the Eulerian model is used directly to solve the two-phase flow field, the water phase volume fraction around the wire will not be correct. To solve this problem, a negative mass term can be added to the governing equation for each mesh element on the first layer of the wire surface, which can be implemented by the UDF in FLUENT software.

The source terms of each governing equation are as follows:

For the mass conservation equation:

$$\text{source}=-\frac{[\rho\alpha(\vec{u}\cdot\vec{A})]_{\text{cell}}}{V_{\text{cell}}} \tag{4}$$

For the momentum conservation equation in x direction:

$$\text{source}_x=-\frac{[\rho\alpha(\vec{u}\cdot\vec{A})]_{\text{cell}}}{V_{\text{cell}}}\cdot u_x \tag{5}$$

For the momentum conservation equation in y direction:

$$\text{source}_y = -\frac{[\rho\alpha(\vec{u}\cdot\vec{A})]_{\text{cell}}}{V_{cell}}\cdot u_y \tag{6}$$

where α represents the water volume fraction, u the velocity of water droplets, subscript cell the control volume, $\vec{A}$ the area vector of the control volume, and V is the volume of the cell.

The calculation of local collection coefficients is very important for icing simulation, and the formula can be used as follows:

$$\beta = \frac{\alpha}{\alpha_\infty}\cdot\frac{\vec{u_d}\cdot\vec{n}}{u_\infty} \tag{7}$$

where α_∞ and u_∞ are the volume fraction of water and velocity of the airflow, respectively. u_d represents the velocity near the wall and $\vec{n}$ is the normal vector of the corresponding wall.

In this study, the two-dimensional icing simulation on the circles and the ellipses is mainly based on the Messinger model (Messinger, B. L.1953). As shown in Figure 6, a micro control volume generally contains air, water and ice.

Figure 6 The mass conservation in control volume

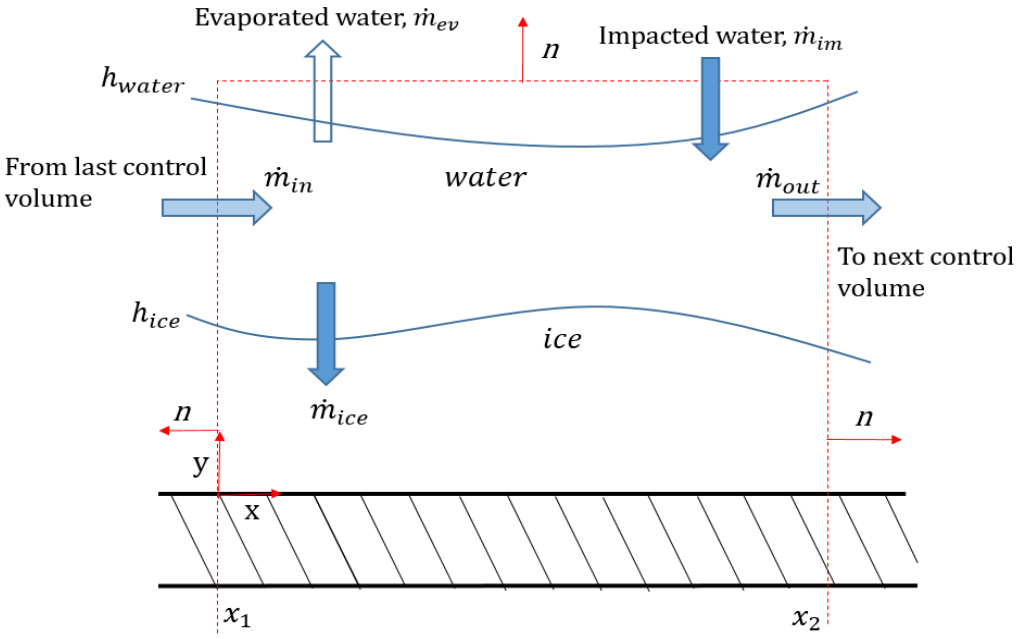

In the control volume, the amount of water entering is always equal to that of the water flowing out and icing. The mass conservation equation is thus obtained as follows:

$$\dot{m}_{\text{im}} + \dot{m}_{\text{in}} = \dot{m}_{\text{ice}} + \dot{m}_{\text{ev}} + \dot{m}_{\text{out}} \tag{8}$$

Where $\dot{m}_{\text{im}}$, $\dot{m}_{\text{in}}$, $\dot{m}_{\text{out}}$, $\dot{m}_{\text{ev}}$ and $\dot{m}_{\text{ice}}$ represents the mass of water impacted into control volume, flow into control volume from the previous control body, outflow to the next control body, evaporated and iced in control volume respectively.

Similarly, the energy in the control body is also conserved and the function as follows:

$$\dot{Q}_{\text{im}} + \dot{Q}_{\text{in}} + \dot{Q}_{\text{ice}} = \dot{Q}_{\text{ev}} + \dot{Q}_{\text{con}} \tag{9}$$

where $\dot{Q}_{\text{im}}$, $\dot{Q}_{\text{in}}$, $\dot{Q}_{\text{ice}}$, $\dot{Q}_{\text{ev}}$ and $\dot{Q}_{\text{con}}$ represent the energy changes caused by water droplets impact, inflow from the previous control volume, outflow to the next control volume, evaporation and icing in control volume, respectively.

The icing coefficient *f* is one of the important parameters for icing simulation and it is defined as the amount ratio of the iced water to the collected water at unit time:

$$f = \frac{\dot{m}_{\text{ice}}}{\dot{m}_{\text{im}} + \dot{m}_{\text{in}}} \tag{10}$$

In this study, the circles and ellipses surfaces were divides into many micro control volumes. Staring from the control volume containing stagnation point and assuming that $\dot{m}_{\text{in}} = 0$ in it, the freezing coefficient of each control volume was calculated with the mass and energy conservation equations of Messinger model.

After the ice mass is obtained, the coordinates of the control volume nodes can be calculated and the ice grows along the normal direction. Consequently, the two-dimensional ice shape can also be obtained after the coordinates of the nodes have been smoothed.

4. Results and discussion

In the current study, prior to the aimed simulation, a two-dimensional icing modelling is introduced in order to develop a three-dimensional model that will be validated against the experimental data. Afterwards, the effects of several different control parameters such as liquid water contents, airflow velocities and water droplet diameters on the pressure loss will be evaluated based on the validated three-dimensional modelling.

4.1 Two-dimensional icing simulation

For the simplified circles and ellipses, as shown in Figure 3, 2D icing simulation with the multi-step method was performed. The boundary conditions and the solution parameters for one of the case studies are described as follows. The inlet boundary condition was set with the airflow velocity of 77 m/s, the volume fraction of water droplets 7×10^{-7}, the liquid water droplet diameter 20 μm, the ambient temperature -5 °C, and the flight altitude being 1,200 m. The outlet boundary condition was set to outflow and the pressure was the ambient pressure. Figure 7 presents the ice shapes of 2D simplified circles for 30° and 4° partitions, respectively. For 20° and 82° partitions, the ice shape changes at each time show a similar trend with that in 30° partition.

Figure 7 Ice shapes of simplified circles at different times in 30°and 4°partitions

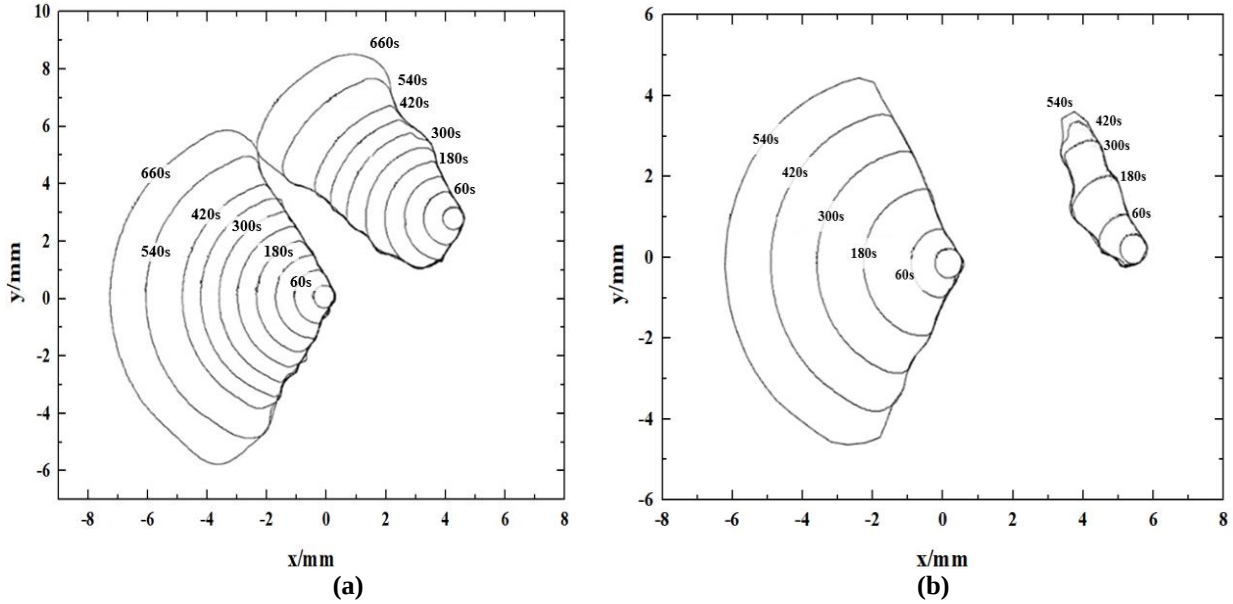

Notes: (a) 30° partition; (b) 4° partition

As shown in Figure 7 (a), when the icing time is shorter than 180 s, the icing of the two circles on the 30° partition show the same ice shape. The icing height reaches almost 2.5 mm at 180 s. However, the ice shape of the left circle would change the flow field when the time is longer than 180 s. It shelters the water droplets and further changes the droplet trajectory characteristics on the right circle. Thus, it can be seen clearly that the mass of the ice decreases in the front of the right circle. With the increase of the icing time, the ice height on both circles continue to increase. It is at approximately at 660 s that the two ice shapes start to meet, indicating that the wire mesh is completely plugged through which the airflow could not pass. Finally, the left circle significantly has more ice formed mass than the right circle. The heights of the icing on the left and right circles are approximately 8.0 mm and 7.0 mm, respectively.

In Figure 7 (b), it could be clearly seen that the ice shapes on the left circle in the 4° partition do not touch those on the right circle. The ice mass on the left circle is considerably larger than that on the right circle. For the case of 4° partition, the two circles are at nearly the same level. A wake region is formed after the air flowed around the left circle. The flow field distribution in front of the right circle is different from that of the left circle. Thus, the droplet trajectory characteristics on the right circle are different. The ice mass is obviously different from that of the left circle. When the icing time is 540 s, the icing height on the left circle reaches approximately 6.5 mm, while that on the right circle is only about 1.5 mm. It can be found that the ice shape on the left circle has a great influence on the icing of right circle. After 540 s, the ice shape of the right circle does not increase.

Figure 8 shows the ice shapes on the ellipses for the cases of 4° partition and 30° partition. From Figure 8, the ice shapes on both ellipses shows nearly the same distribution at each time. It could be the reason that the two ellipses cannot shelter each other. Consequently, the flow field distribution is identical around both ellipses. In addition, it takes 280 s and 260 s, respectively, for the ellipses icing in the two partitions to block the mesh completely, which are significantly shorter than the blocking time on the circles. Similar cases also occur in partitions of other angles. The time for ice to completely block the mesh in each partition is approximately determined by the icing of the ellipse. Therefore, the blocking time in different partition is almost the same and it can be considered as the blocking time of whole protection net.

Figure 8 Final ice shapes of ellipses in 4°and 30°partitions

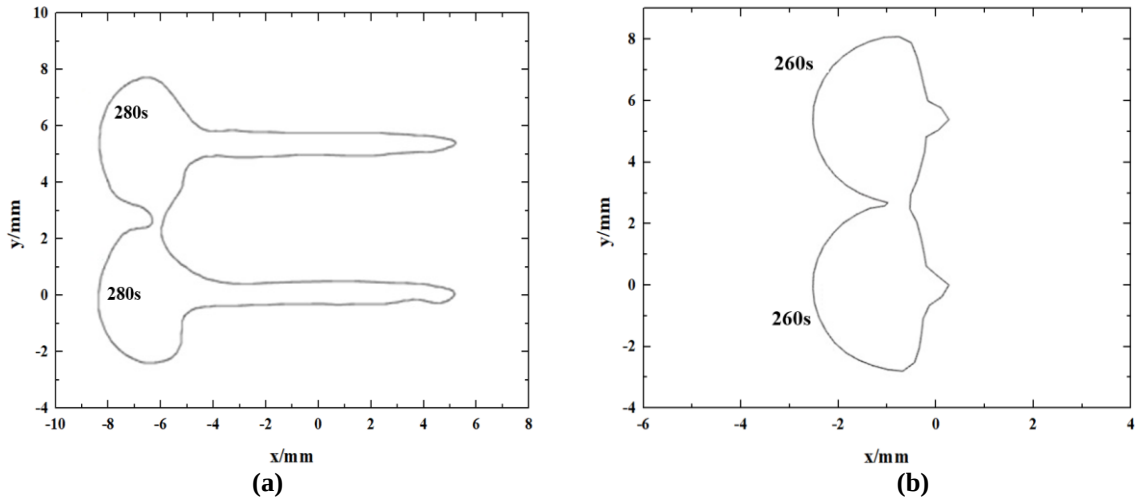

Notes: (a) 4° partition; (b) 30° partition

4.2 Comparison between experimental data and simulation results of icing

Figure 9 presents the ice shapes on the protection net under different conditions in the icing wind tunnel. The icing conditions are listed in Table 1. It can be clearly seen from Figure 9 that the ice shapes show obvious differences in various cases. In Figure 9 (a), the entire protection net is covered by a thin layer of ice and the meshes are blocked. In this case, the growth rate of icing is small due to the lower airflow velocity of 11 m/s. During the whole experiment, no ice dropping is observed. However, it is noted that the ice falls off from the protection net during the tests for the cases of 2 and 3. It can be found from Figure 9 (b) that the height of a part of ice is approximately 1.5 cm for the case of 20^{o} partition. Due to the low temperature of -30 ℃, the rime ice is formed. In Figure 9 (c), the ice on the protection net is made up of glaze ice with a larger ice height. As a result, the air flow field at the engine intake is changed since the protection net is blocked by the ice.

It should be noted that the ice shape on protection net can only be measured after the experiment being finished. The air temperature in the icing tunnel has increased and the ice continues to melt, and even some parts of ice has dropped. Therefore, the measured ice shapes are different from that during the experiment, and the ice shapes between simulation and experiment results will not be discussed in this paper.

Figure 9 Ice shapes on protection net in different cases after the experiment

(a)

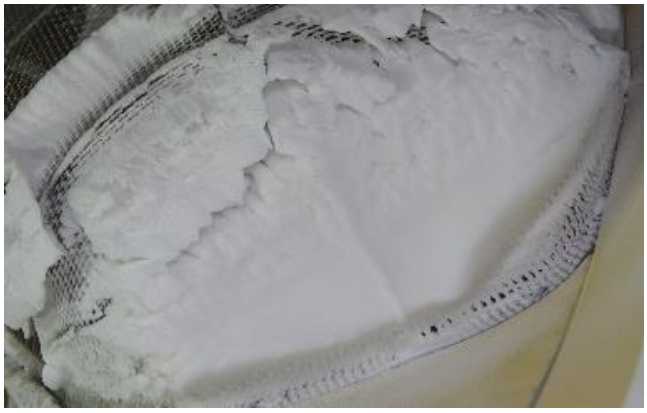

(b)

(c)

Notes: (a) Ice shape of case 1 in Table1; (b) Ice shape of case 2 in Table1; (c) Ice shape of case 3 in Table1

The pressure loss of the protection net due to icing can be measured through the icing wind tunnel experiments. Additionally, the data of pressure loss is also presented by the above proposed numerical method. Figure 10 shows the pressure losses at different times measured by the experiment and the simulation for the cases of 1 and 2, as listed in Table 1. In the experiment, the time before the spray is about 5s and it is regarded as the time to start the pressure loss measurement. At this time, t = 0s, there is no ice in protection net. In addition, in the simulation, the time steps of the multi-step method for the cases of 1 and 2 are set to 100 s and 15 s, respectively. It can be clearly seen from Figure 10 that the pressure loss continued to increase over time. Since the air flow velocity in case 2 is larger than that in case 1, the amount of icing on the protection net in case 1 is larger than that in case 2 during the same period of time. Thus, the pressure loss caused by icing in case 2 increases more rapidly than that in case 1. Furthermore, the comparison between the experimental data and simulation results shows that they are in good agreement, which further verifies the numerical method that proposed in the current study.

Figure 10 Pressure losses at different times in experiment and simulation for cases 1 and 2

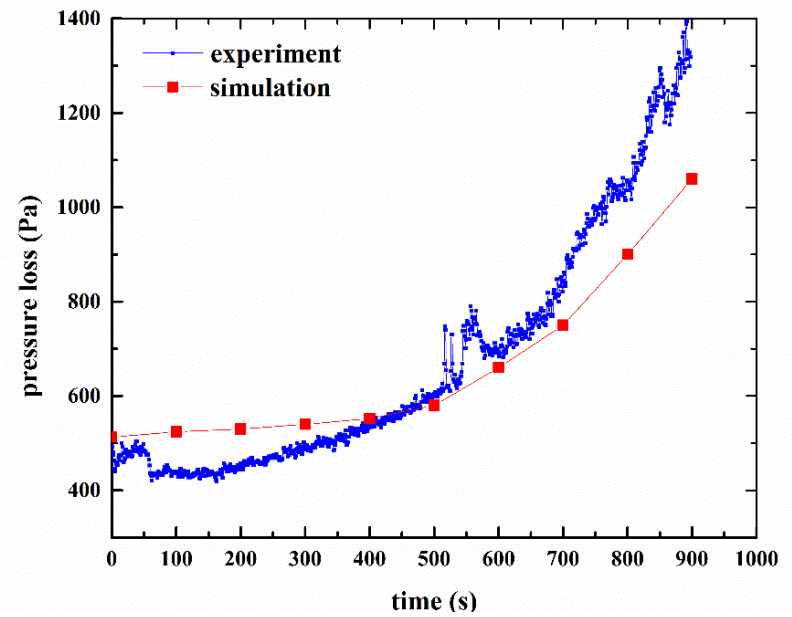

(a)

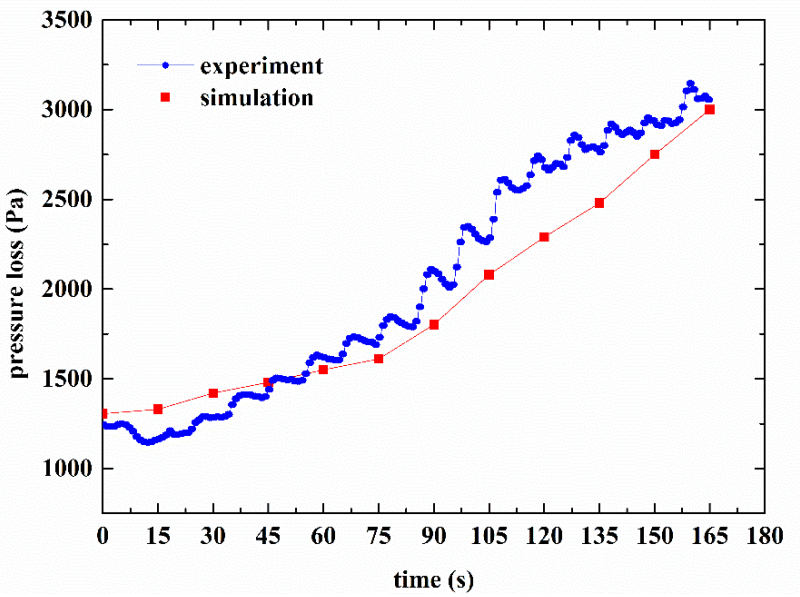

(b)

Notes: (a) Results of case 1; (b) Results of case 2

In Figure 10 (a), the pressure losses at initial time measured by the experiment and the simulation are 493 Pa and 513 Pa, respectively. The error of 4.06% indicates that the porous media model used to simplify the protection net has high accuracy. In the icing process, the growth rate of the pressure loss before 400 s is slower than that after 400 s.

The reason could be explained as follows. During the initial stage of the icing, the ice on the protection net grows slowly and the effect of the ice on the air flow field is not significant. With the increase of the icing time, the amount of ice increases, causing an obvious decrease in the mesh area of the pressure net. Therefore, the flow field is changed and the pressure loss increases. At the ten time-steps of icing process, the average error between the simulation and experimental results is 10.53%.

As shown in Figure 10 (b), the pressure losses resulted from the experiment and the simulation are 1243 Pa and 1305 Pa at the initial time with an error of 4.99%. The growth rate of the pressure loss before 75 s is smaller than that after 75 s. Compared with the pressure loss in case 1, it shows a much more rapid increase. It could be caused by the large airflow velocity in case 2. The higher the air flow velocity, the larger the droplet collection coefficient and the icing quantity. In the icing process, the average error between the simulation and experimental results is 8.31%. The comparison results of pressure loss in case1 and case2 demonstrates the validity and rationality of the simulation method in current study.

4.3 The effect of control parameter on the pressure loss

Having completed a preliminary validation of the numerical simulation, this section will investigate whether the model behaves reasonably in a wider variety of conditions. The effects of different liquid water contents, airflow velocities and water droplet diameters on the pressure loss caused by the iced protection net are analyzed. In the simulation, the time step of the multi-step method is 100 s, and the total calculation time is 800 s.

4.3.1 Different LWCs

Figure 11 presents the variation of the pressure loss with the icing time under three different LWCs of 0.4 g/m^3, 0.6 g/m^3, and 0.8 g/m^3. The temperature and velocity of the air are -5 ℃ and 11 m/s, respectively. The mass flow rate is 3.97 kg/s. The MVD is 20 μm.

Figure 11 Changing trend of pressure loss with icing time under three different LWCs

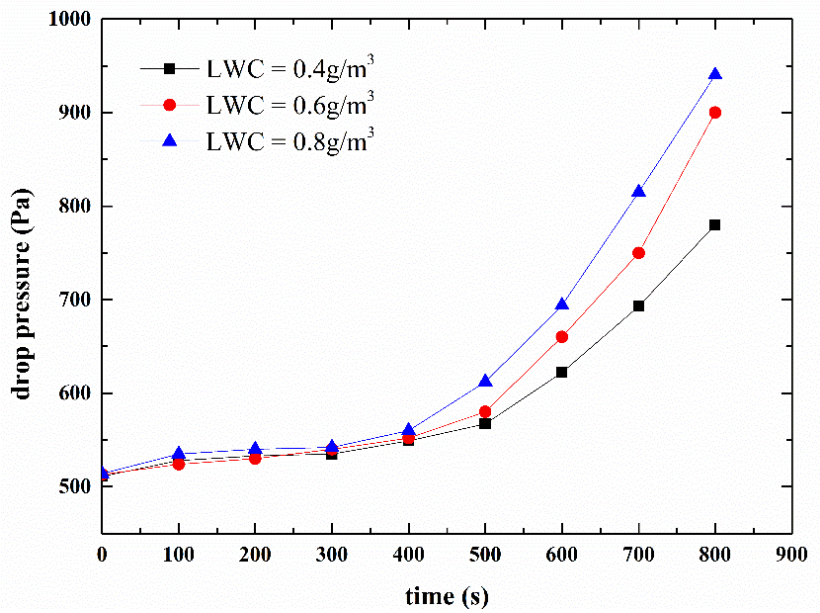

As shown in Figure 11, the higher the LWC, the higher the pressure loss, which is more obvious as the icing time increased. At the initial time, the pressure loss is about 513 Pa under the three different LWC conditions, indicating that the LWC change has a little effect on the pressure loss. Then, the pressure loss shows a slight change before 400 and it increases rapidly after 400s. For example, when LWC is 0.4 g/m^3, the pressure loss increases from 511 Pa to 549 Pa from 0 s to 400 s. But from 400 s to 800 s, the pressure loss increases from 511 Pa to 780 Pa, that is signification larger increase gradient. The reason for this change has been explained in Section 4.2. For a large LWC particularly, more water droplets are captured and the amount of ice increases, which could cause more rapid decrease of the mesh area. Consequently, the pressure loss shows a higher value for a higher LWC.

4.3.2 Different diameters of water droplets

The pressure loss curves of the protection net at different icing times under three different MVDs of 15μm, 20μm and 25μm are shown in Figure 12. The temperature and velocity of the air are -5 ℃ and 11 m/s, respectively. The mass flow rate is 3.97 kg/s. The LWC is 0.6 g/m^3. It can be seen from Figure 12 that the pressure loss rises with the icing time under three different MVDs. The pressure losses also show a slower growth before 400 s than that after 400 s. The reason can refer to the explanation of the effect of different LWCs on pressure loss. Furthermore, the pressure loss value does not change significantly with the increase of droplet diameter. The difference between 15 μm diameter and 20 μm diameter, 20 μm diameter and 25 μm diameter are 2 Pa and 6 Pa at 400 s. At 800 s, they are 43 Pa and 23 Pa, respectively.

Figure 12 Curves of pressure losses with icing time under three different MVDs

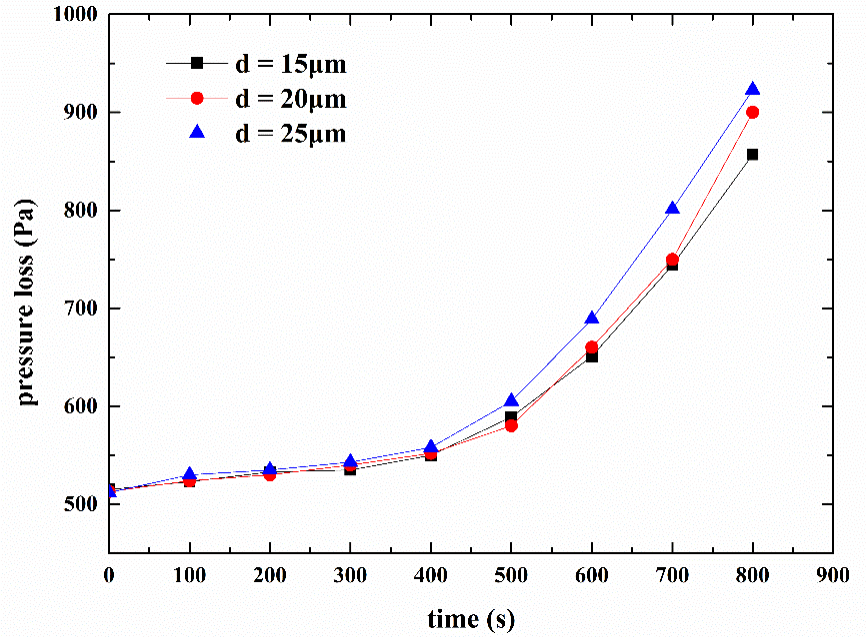

4.3.3 Different airflow velocities

Figure 13 presents the profile of the pressure loss with the icing time under three different velocities of 11 m/s, 12 m/s and 13 m/s. The temperature and the LWC of the air are -5 ℃ and 0.6 g/m^3. The mass flow rate is 3.97 kg/s. The MVD is 20 μm.

Figure 13 Curves of pressure losses with icing time under three different velocities

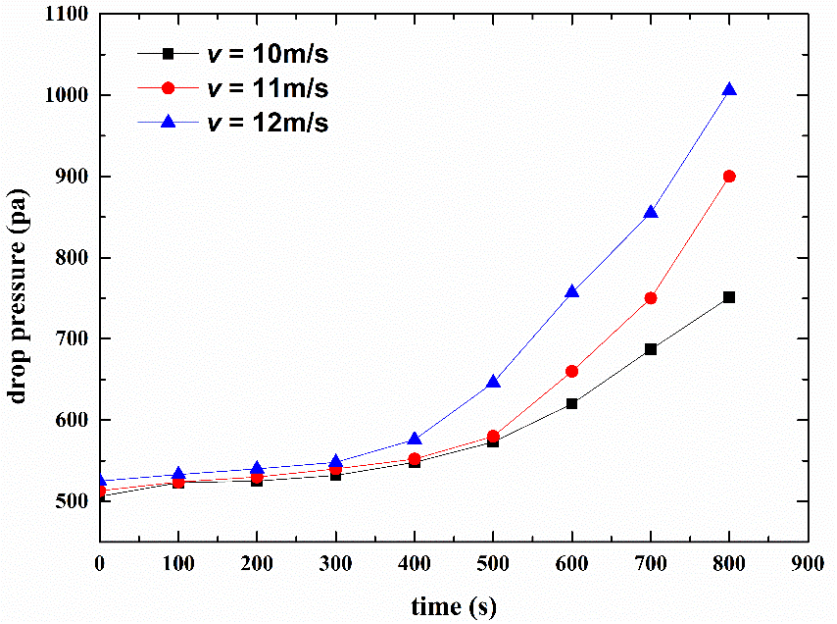

It can be clearly seen from Figure 13 that the higher the velocity, the higher the pressure loss. The trend is more evident when the icing time is beyond 400 s. Due to the differences of airflow velocity, the pressure losses at 10 m/s, 11 m/s, and 12 m/s at the initial time are 506 Pa, 513 Pa, and 525 Pa, respectively. This is because the change in velocity has a considerable effect on the pressure field. In addition, at 10 m/s, 11 m/s and 12 m/s, the pressure losses at 800 s are 751 Pa, 900 Pa and 1006 Pa, respectively. The reason could be that the higher the air flow velocity, the larger the droplet collection coefficient and the icing quantity. As a result, the pressure loss is higher.

It is convenient to characterize the fluid resistance of iced protection net with a dimensionless quantity K_l, which is called the loss factor and can be determined:

$$K_l = \frac{2\,\Delta P}{\rho\, v^2} \tag{11}$$

Figure 14 shows the variations of K_l of iced protection net over time at airflow velocities of 10 m/s, 11 m/s and 12 m/s. Consistent with the trend of pressure drop, the value of K_l increases with time at each airflow velocity. It can be explained by the fact that with the growth of icing, the protection net is more plugged, resulting in the increase of K_l. In addition, the higher the velocity, the smaller the K_l at a certain time. And the difference of K_l decreases over time.

Figure 14 The variations of the loss factor versus the time for different velocities.

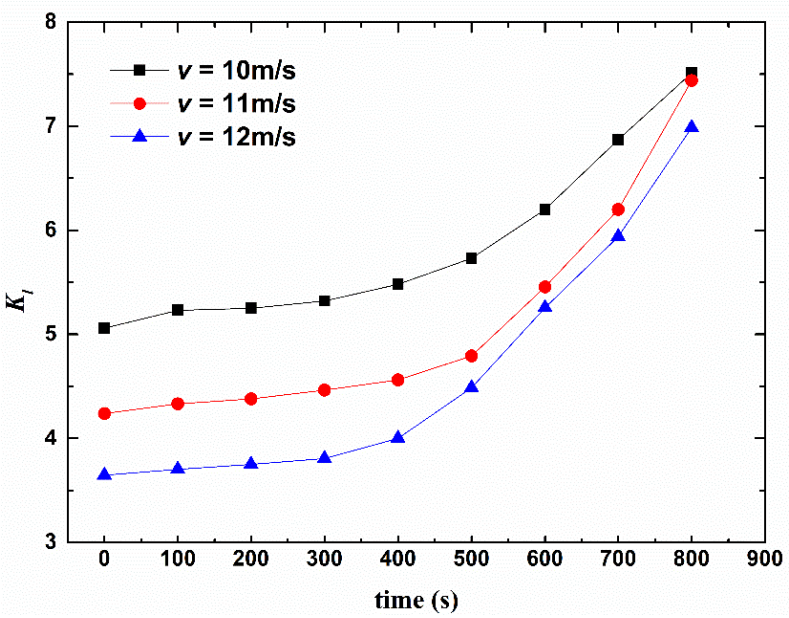

5. Conclusions

In the current work, a combined numerical and experimental investigation was conducted to study the icing of the protection net of the helicopter engine inlet. A new predicting method for net-like structure icing and the consequent pressure loss was addressed. The influence of various parameters such as the LWC, the diameter of water droplets and the airflow velocity was analyzed using the validated modelling. Major findings based on the numerical and experimental results are as follows.

(1) For the 2D simplified wire mesh, the icing leading to complete mesh blocking take different times on both circles and ellipses in different partitions. The icing time for entire blocking in each partition is approximately identical, i.e, the whole protection net almost simultaneously reaches complete blocking. The icing height shows different values in different partitions of the protection net. For the 3D iced protection net, the pressure loss increases with the icing time before the mesh is completely blocked. Particularly in the later period of icing, the pressure loss shows a faster upward trend.

(2) The ice shape, icing quantity, and consequent pressure loss are markedly different in three different cases in the icing wind tunnel experiments. In the two simulation cases, the average error between simulation results and experiment results is 10.53 % and 8.31 % respectively. That indicates the correctness and validity of the simulation method to predict the pressure loss of the iced protection net in this study, and the method can contribute to the icing simulation of net-like structures.

(3) When other icing parameters are the same, the higher the LWC, diameter of water droplets and the airflow velocity, the higher the pressure loss of the protection net. It is more evident as time increases, and the pressure loss sharply increases after 400s. In the icing conditions LWC 0.4 g/m3, temperature -5 ℃ and velocity 11 m/s, the pressure loss increases from 511 Pa to 549 Pa from 0 s to 400 s. But from 400 s to 800 s, the pressure loss increases from 511 Pa to 780 Pa. The later has a signification larger increase gradient. For the loss factor, the value of K_l increases with time at each airflow velocity. And the higher the velocity, the smaller the K_l at a certain time.

References.

Wilcox, M. Kurz, R. Brun, K. (2012). “Technology review of modern gas turbine inlet filtration systems”. *International Journal of Rotating Machinery*, 2012, 1-15.

Ikiades, A. A., Spasopoulos, D., Amoiropoulos, K., Richards, T., Howard, G., Pfeil, M. (2013). “Detection and rate of growth of ice on aerodynamic surfaces using its optical characteristics”, *Aircraft Engineering and Aerospace Technology,* Vol. 85. No. 6, pp. 443-452.

Gao, L., Liu, Y., Hu, H. (2019). “An experimental investigation of dynamic ice accretion process on a wind turbine blade model considering various icing conditions”. *International Journal of Heat and Mass Transfer*, 133, 930-939.

Li, L., Liu, Y., Zhang, Z., Hu, H. (2019), “Effects of thermal conductivity of airframe substrate on the dynamic ice accretion process pertinent to UAS inflight icing phenomena”, *International Journal of Heat and Mass Transfer,* vol. 131, pp.1184-1195.

Vercillo,V. , Karpen,N. , Laroche,A., et al. (2019). “Analysis and modelling of icing of air intake protection grids of aircraft engines”. *Cold Regions ence and Technology*, 160(APR.): 265-272.

Jin, J. Y., Virk, M. S. (2020). “Experimental study of ice accretion on s826 & s832 wind turbine blade profiles”. *Cold regions ence and technology*, 169(Jan.), 102913.1-102913.8.

Du, Y., Gui, Y., Xiao, C., Yi, X. (2010), “Investigation on heat transfer characteristics of aircraft icing including runback water”, *International Journal of Heat and Mass Transfer,* Vol. 53, No. 19-20, pp. 3702-3707.

Verdin, P. G., & Charpin, J. P. (2013), “Multi-stepping ice prediction on cylinders and other relevant geometries”, *Journal of Aircraft,* Vol. 50, No. 3, pp. 871-878.

Pouryoussefi, S. G., Mirzaei, M., Nazemi, M. M., Fouladi, M., Doostmahmoudi, A. (2016), “Experimental study of ice accretion effects on aerodynamic performance of an NACA 23012 airfoil”, *Chinese Journal of Aeronautics,* Vol. 29, No.3, pp. 585-595.

Raj, L, P, Lee, J. W., Myong, R. S. (2019), “Ice accretion and aerodynamic effects on a multi-element airfoil under SLD icing conditions”, *Aerospace Science and Technology,* Vol. 85, pp. 320-333.

Chang, S., Leng, M., Wu, H., Thompson, J. (2016), “Aircraft ice accretion prediction using neural network and wavelet packet transform”, *Aircraft Engineering and Aerospace Technology: An International Journal,* Vol. 88, No. 1, pp. 128-136.

Zhang, X, Wu. X, Min, J. (2017), “Aircraft icing model considering both rime ice property variability and runback water effect”, *International Journal of Heat and Mass Transfer,* Vol. 104, pp. 510-516.

Groth, C., Costa, E., Biancolini, M. E. (2019). “Rbf-based mesh morphing approach to perform icing simulations in the aviation sector”. *Aircraft engineering*, 91(4), 620-633.

Son, C., Kim, T. (2020). Development of an icing simulation code for rotating wind turbines. *Journal of Wind Engineering and Industrial Aerodynamics*, 203, 104239.

Li, S., Qin, J., He, M., Paoli, R. (2020). “Fast evaluation of aircraft icing severity using machine learning based on xgboost”. *Aerospace*, 7(36).

Castellano, S., Starace, G., De, Pascalis. L., Lippolis, M., Mugnozza, G. S. (2016), “Test results and empirical correlations to account for air permeability of agricultural nets”, *Biosystems Engineering,* Vol. 150, pp. 131-141.

Cheung, S. W., Chung, E. T., Efendiev, Y., Gildin, E., Wang, Y., Zhang, J. (2019). “Deep global model reduction learning in porous media flow simulation”. *Computational Geosciences,* 24:261–274

Pashchenko, D., (2019). “Pressure drop in the thermochemical recuperators filled with the catalysts of various shapes: a combined experimental and numerical investigation”. *Energy*, 166:462-470

Movahedi, H., Farahani, M. V., & Masihi, M. (2020). “Development of a numerical model for single- and two-phase flow simulation in perforated porous media”. *Journal of Energy Resources Technology*, 142(4), 042901.1-042901.12.

Montoya, D., Jahn, W., & Rivera, J. D. D. (2020). “Using a porous medium model to simulate the air flow through fog water collectors”. *Journal of Porous Media*, 23(6).

SAE Aerospace. Calibration and acceptance of icing wind tunnels: SAE ARP5905[S]. SAE, 2003.

Messinger, B. L. (1953), “Equilibrium Temperature of an Unheated Icing Surface as a Function of Air Speed,” *Journal of the Aeronautical Sciences,* Vol. 20, No. 1, pp. 29–42.

Fluent A. Fluent 14.0 user’s guide [J]. ANSYS FLUENT Inc, 2011.